Nuclear Materials and Energy 49 (2026) 102229

Contents lists available at ScienceDirect

Nuclear Materials and Energy

journal homepage: www.elsevier.com/locate/nme

Experimental analysis of Pt marker erosion in the outer divertor region of ASDEX Upgrade during L- and H-mode discharges☆

S. Saari [a,*], A. Hakola [a], J. Karhunen [a], K. Krieger [b], M. Rasinski [c], M. Balden [b], C. Baumann [c], I. Bogdanović Radović [d], S. Gouasmia [d], M. Mayer [b], G. Provatas [d], J. Romazanov [c], ASDEX Upgrade Team[1], EUROfusion Tokamak Exploitation Team[2]

[a] VTT Technical Research Centre of Finland, 02150 Espoo, Finland
[b] Max-Planck-Institut für Plasmaphysik, 85748 Garching, Germany
[c] Forschungszentrum Jülich GmbH, Institute of Fusion Energy and Nuclear Waste Management - Plasma Physics, 52425 Jülich, Germany
[d] Ruđer Bošković Institute, HR-10000 Zagreb, Croatia

ARTICLE INFO

Keywords:
Divertor erosion
Material migration
ASDEX Upgrade
Marker samples

ABSTRACT

Erosion and material migration of W at the outer divertor target of ASDEX Upgrade were investigated under controlled plasma conditions. Experiments were carried out using small Pt markers as proxy for W, placed on Mo substrate, together with bulk W and Mo samples. The samples were exposed to L-mode and H-mode plasmas. Post-exposure analysis was performed using ion beam analysis techniques and scanning electron microscopy (SEM). In H-mode, the Pt marker data showed distinct erosion peaks in the scrape-off layer (SOL) adjacent to the outer strike point (OSP), and deposition regions in the near SOL. In contrast, L-mode samples exhibited less distinct erosion near the OSP, and overall a 2–6 times lower net erosion rate. The observed qualitative differences may be related to transport processes and variations in ionisation mean free paths. Micro-proton-induced X-ray emission (μPIXE) measurements indicate spatially resolved Pt deposition patterns in the SOL consistent with transport driven by parallel plasma flow and radial transport processes, accumulating both downstream from the markers and towards the OSP. W measured at the same locations exhibited more uniform surface distribution, but remains associated with regions showing visible surface modifications, which may be related to reduced effective sputtering and enhanced local re-deposition within surface features. Nuclear reaction analysis (NRA) and energy-dispersive X-ray spectroscopy (EDX) indicate the accumulation of light impurities, including O, B, C, D and N, in surface layers near the OSP. The results highlight the role of surface modification and SOL transport in shaping impurity migration patterns.

1. Introduction

Tungsten (W) is regarded as a good candidate material for plasma facing components (PFCs) in future tokamak reactors due to its ability to withstand high thermal loads and neutron irradiation while exhibiting relatively low hydrogen retention [1]. However, understanding net and gross erosion of W due to sputtering is crucial in order to maximise the lifetime of reactor walls and ensure reliable operation. This requires knowledge not only of the erosion rates of PFCs, but also of the subsequent migration of the eroded material, its deposition patterns, and how effectively W is transported and screened at different locations. Experimental data is also essential to benchmark modelling tools, enabling simulations to be extended to reactor-relevant volumes and supporting the design of future fusion power plants.

A well-established method for studying these processes is the exposure of dedicated marker samples to plasma, followed by analysis of their modifications after the experiment. This approach was pioneered in experiments on the JET [2] and has since been adopted in several other devices, including ASDEX Upgrade (AUG) [3], which is a full-W tokamak [4] designed to investigate plasma confinement, stability, and exhaust relevant for ITER and future fusion reactors [5]. It is also equipped with the DIM-II [6], a dedicated manipulator system

☆ This article is part of a Special issue entitled: 'PSI-27 Proceedings' published in Nuclear Materials and Energy.

* Corresponding author.
E-mail address: samuli.saari@vtt.fi (S. Saari).

[1] See author list of T. Pütterich et al. 2026 Nucl. Fusion 66 116002 https://doi.org/10.1088/1741-4326/ae61c8.

[2] See the author list of N. Vianello et al "Results from the last DD and DT JET campaigns in the framework of the EUROfusion Tokamak Exploitation Work Package Activity" 2026 Nucl. Fusion in press https://doi.org/10.1088/1741-4326/ae71ec.

https://doi.org/10.1016/j.nme.2026.102229
Received 17 July 2026; Received in revised form 15 September 2026; Accepted 1 October 2026
Available online 7 October 2026
2352-1791/© 2026 The Authors. Published by Elsevier Ltd. This is an open access article under the CC BY license (http://creativecommons.org/licenses/by/4.0/).

Table 1
Key parameters for plasma discharges of the experiment. Here EC stands for electron cyclotron resonance heating and NI stands for neutral beam injection.

Experiment type and discharge numbers	Gas	Plasma current (MA)/ Toroidal field (T)	Core density (10^{19} m^{-3})	Heating power EC/NI (MW)	Total flat-top time (s)
H-mode: #43541–43545	D, Ne	0.8/−2.5	6.4–6.9	NI 2.5, EC 1.5	31.4 s
L-mode: #43566–43568	D, Ne	0.8/−2.5	5.2–5.8	EC 0.7	12.8 s
L-mode: #43569–43570	D	0.8/−2.5	5.3–5.4	EC 0.7	10.5 s

in the divertor region, allowing the insertion and retrieval of marker samples in the outer divertor between experimental days. This enables short-term exposure of marker samples to individual discharges while maintaining relatively steady conditions compared to exposure over a full campaign.

The present paper reports in detail an experiment in which platinum (Pt) marker samples on molybdenum (Mo) substrates were mounted near the outer strike point (OSP) and exposed to AUG plasma discharges with Pt acting as a proxy material for W. Different sets of bulk W and Mo samples were exposed simultaneously. The aim of the experiment was to investigate net erosion and deposition rates on PFCs, as well as material migration on the outer divertor target.

2. Experiment

In the experiment, Pt markers on a Mo substrate, together with bulk Mo and W samples, were exposed to H- and L-mode deuterium (D) plasmas in the OSP region of the AUG. The experiments were carried out with the aim of maintaining a similar magnetic geometry for both H-mode and L-mode plasmas. The samples were subjected to five L-mode and five H-mode discharges on consecutive experimental days. The key parameters of the discharges are presented in Table 1.

Neon (Ne) seeding was applied in the divertor with the intention to enhance the erosion of samples, but the injected Ne amounts were very low due to operational limitations, and their influence is assumed to be negligible for the purpose of the analysis. In H-mode, minor Ne injection was applied at the end of the flat-top phase in all five discharges. The total sample exposure time, including ramp-up and ramp-down phases, was 40.6 s, with a cumulative flat-top duration of 31.4 s. For L-mode, Ne injection was initially applied during the first three discharges but was either unsuccessful or led to prompt disruptions and was therefore omitted in the subsequent discharges (see Table 1). For the L-mode discharges, the total sample exposure time was 30.3 s, with a cumulative flat-top duration of 23.3 s.

2.1. Samples

The size of the Pt samples, as well as the bulk Mo and W samples, was constrained by predefined slots in dedicated W divertor tiles, which were subsequently inserted into the OSP region using the DIM-II divertor manipulator. Five adjacent Pt samples and six Mo and W samples were mounted per row, as illustrated in Fig. 1 together with the numbering of the samples. Two parallel rows of samples were mounted on dedicated divertor manipulator tiles with the Pt marker layers of different thicknesses on one tile and the Mo and W samples on another, as shown in Fig. 2(a) and (b), respectively. In total, four Pt sample sets were used, referred to here as L-30, L-120, H-30, and H-120, where the letter denotes the plasma mode and the number the Pt marker thickness in nm. The bulk Mo and W sample sets are referred to as Mo and W samples (or Mo/W samples when both sets are considered), with the prefixes L-mode or H-mode used when necessary. In this article, the term *Pt sample* refers to the Mo substrate with Pt markers, whereas *Pt markers* refer to the thin Pt layers on the Mo substrate.

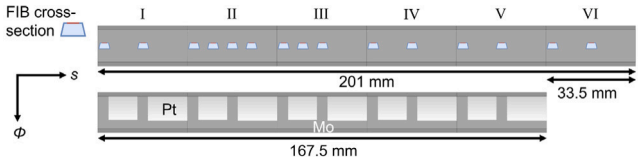

Fig. 1. A single W/Mo sample set together with a Pt sample set. The FIB cross sections on the Mo/W sample set are not to scale for illustrative purposes. The *s* coordinate measures distance along the wall surface, increasing from the OSP towards the outer midplane.

2.1.1. Pt samples

Candidate proxy materials for W were selected from metals with atomic number and mass close to those of W (Z_W = 74, m_W≈184 u). W-like mass was regarded as an important requirement, as it results in a comparable gyroradius for singly ionised particles and therefore similar prompt gyro-re-deposition behaviour under divertor conditions. Among these, Pt (Z_{Pt} = 78, m_{Pt}≈195 u) has a relatively low oxidation tendency compared to several non-noble transition-metal alternatives with masses close to W [7], namely rhenium (Re, Z_{Re} = 75, m_{Re}≈186 u) as well as lighter lutetium (Lu, Z_{Lu} = 71, m_{Lu}≈175 u), hafnium (Hf, Z_{Hf} = 72, m_{Hf} ≈178 u) and tantalum (Ta, Z_{Ta} = 73, m_{Ta} ≈181 u). It is also safer to handle than toxic osmium (Os, Z_{Os} = 76, m_{Os} ≈190 u) [8]. In addition, its thin film properties are more favourable than those of iridium (Ir, Z_{Ir} = 77, m_{Ir} ≈192 u), which are strongly dependent on processing conditions, leading to significant variations in microstructure and surface morphology [9]. In preliminary modelling studies performed using the ERO2.0 code [10], the erosion rate of Pt was found to be noticeably closer to that of W than was the case for the previously used gold (Au, Z_{Au} = 79, m_{Au} ≈197 u) [11,12].

Each Pt sample consisted of a single Mo substrate (surface area 33.5 × 12 mm^2) with two thin Pt markers on top, as illustrated in Fig. 3. The use of Mo as a substrate enables easier quantification of Pt deposited from material eroded from the markers and, more importantly, quantification of W deposited from the surrounding environment and neighbouring tiles. The marker dimensions of 10.75 × 9 mm^2 and 14.75 × 9 mm^2 were estimated to provide sufficiently large Pt areas for analysis of net erosion, which in [11] was found to be complicated by toroidal migration of the eroded Au largely outside the applied 5 × 5 mm^2 markers, thereby not reliably capturing net erosion. In addition, the 4 mm wide inter-marker Mo gaps and the 3 mm wide Mo stripe at the downstream edge of the sample in the direction of the parallel plasma flow enabled investigation of Pt migration and re-deposition.

Markers for separate Pt sample sets were manufactured with two nominal thicknesses: 30 nm and 120 nm. The rationale for using markers with two different thicknesses was that the 30 nm markers allow measurement of small erosion, but they may be completely eroded in the regions of high erosion, such as near the OSP. In such cases, the 120 nm markers still allow reliable measurements. Two sample sets with each marker thickness were manufactured, dedicated to the L- and H-mode plasma exposures.

2.1.2. Bulk W and Mo samples

On the bulk W and Mo samples with the same outer dimensions as the Pt samples, focused ion beam (FIB) cross sections with horizontal

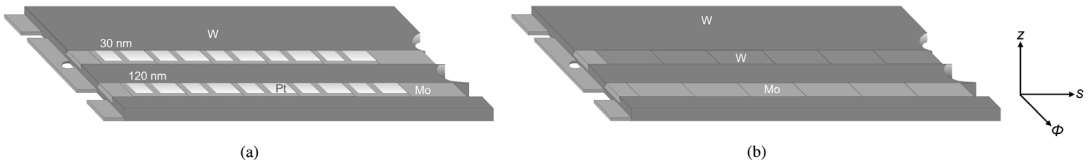

Fig. 2. Schematic illustration of the sample arrangement on the DIM-II manipulator tiles: (a) 30 nm and 120 nm Pt markers and (b) W and Mo samples.

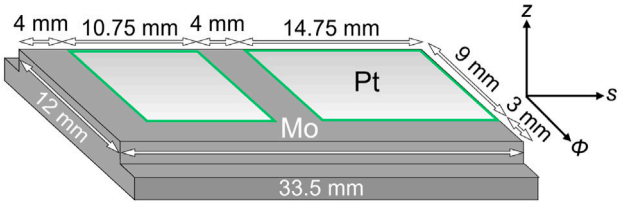

Fig. 3. Schematic illustration of a Pt sample with the edges of the markers highlighted with green.

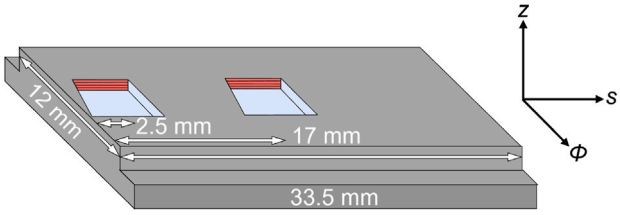

Fig. 4. Schematic illustration of a W/Mo sample with FIB cross sections indicated in blue and red, with red indicating the edge containing the horizontal line markings. The indicated values represent the distances of the centres of the cross sections from the edge of the sample. The FIB cross sections are not to scale for illustrative purposes. In the toroidal direction, the cross sections are located at the centre of the sample.

line markings were prepared to enable subsequent determination of net erosion and deposition by observation of the surface morphology with respect to the line markings using scanning electron microscopy (SEM). The approximate width and depth of the cross sections were 20 μm and 8–10 μm, respectively. The first two line markings were separated by ~1 μm, while the remaining markings were spaced by ~2 μm. A schematic illustration of a cross section sample with the dimensions is shown in Fig. 4, and an example SEM image of the cross section with the markings is presented in Fig. 5.

2.2. Pre-exposure measurements for Pt samples

Before subjecting the Pt samples to plasma discharges, pre-erosion thickness measurements were performed to establish reference values for each marker, enabling determination of post-exposure net erosion. Measurements were conducted at the Tandem Laboratory of Max-Planck-Institut für Plasmaphysik (IPP), Garching, Germany [13], using Rutherford backscattering spectrometry (RBS) with 2 MeV alpha (^{4}He) particles and a total charge of 5 μC. With an incident angle of 0° and an exit angle of 15°, the resulting scattering angle was 165°. For each marker, the thickness was measured at a single location near the centre of the marker, assuming spatially homogeneous thickness of the Pt layer prior to the plasma exposure. The marker layer thicknesses were determined by fitting the resulting RBS spectra using the SIMNRA software [14]. The pre-exposure thicknesses with the corresponding measurement positions are presented in Fig. 6. The measured thicknesses of the marker layers ranged approximately from 20 to 35 nm for the markers with nominal thickness of 30 nm and from 90 to 120 nm for the markers with nominal thickness of 120 nm. In addition, the larger

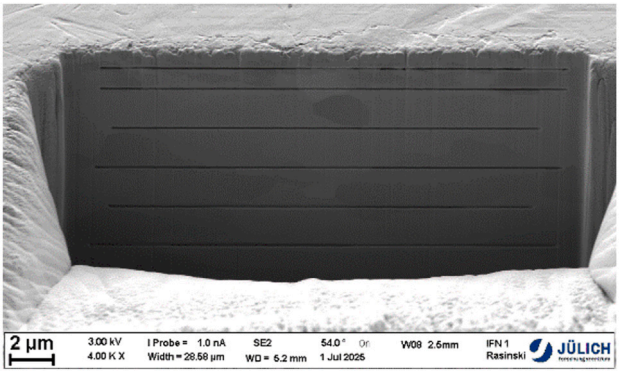

Fig. 5. SEM image of a prepared FIB cross section with horizontal line markings prior to plasma exposure.

marker on a given sample was systematically thicker than the smaller marker.

The uncertainties of the measured RBS thicknesses were estimated by combining counting-statistical and additional uncertainty contributions. The relative statistical uncertainty of the detected peak intensities was assumed to follow Poisson statistics. For a peak containing N counts, the absolute counting uncertainty is $\sqrt{N}$, corresponding to a relative statistical uncertainty of $1/\sqrt{N}$. For RBS, the additional uncertainty contribution, u, accounts for uncertainties associated with the beam current measurement, possible loss of secondary electrons in the Faraday cup and detector calibration. Together, these contributions correspond to an additional relative uncertainty of approximately 5% for RBS. The total relative uncertainty, u_{rel}, was obtained by combining the relevant contributions via standard quadratic error propagation [15].

$$u_{\mathrm{rel}} = \sqrt{\left(\frac{1}{\sqrt{N}}\right)^2 + u^2}. \quad (1)$$

2.3. Post-exposure analysis for samples

2.3.1. Pt sample analysis

In the post-exposure analysis all of the Pt samples were re-analysed using RBS to determine changes in the Pt layer thicknesses during plasma exposure, now covering both the Pt markers and the inter-marker Mo substrate regions using the same 2 MeV ^{4}He beam as in the pre-exposure measurements. In contrast to the pre-exposure measurements, the post-exposure RBS analyses were performed at two or three different s coordinate positions on each marker, depending on the marker dimensions, for improved spatial resolution of the net erosion profiles, as shown in Fig. 7. The initial charge per measurement point was the same as in the pre-exposure measurements.

Proton-induced X-ray emission (PIXE) measurements were performed for samples I–III in all four sample sets at the same positions as the post-discharge RBS measurements shown in Fig. 7. The analyses provided information on the concentrations of high-Z elements on the surfaces, i.e., Pt and deposited W. The measurements were performed using a 1.5 MeV proton beam with a charge of 5 μC per measurement

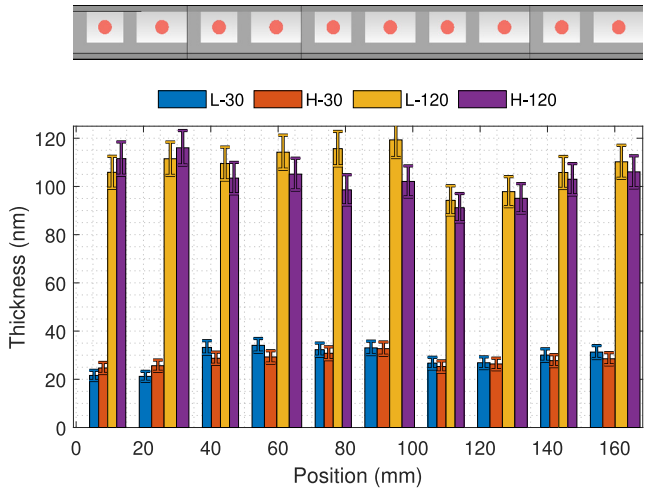

Fig. 6. Pre-exposure thicknesses of the Pt marker layers and their corresponding measurement positions (red dots) along the sample row. At each measurement position, four bars correspond to different sample sets (L-30, H-30, L-120, H-120), with each set indicated by a distinct colour. Alternating bar widths represent the two marker sizes within a single sample.

position. An AXAS-D (KETEK) detector was positioned at 45° with respect to the surface normal and a Mylar absorber with a total thickness of 63.9 μm was used.

Nuclear reaction analysis (NRA) was performed for samples II of the L-120 and H-120 sets to determine the amounts and composition of deposited light elements on the samples in the vicinity of the OSP. Analysis was conducted using 3 MeV ^{3}He ions at the measurement positions presented in Fig. 7. The samples were selected based on visual inspection which revealed a distinct dark surface region near the OSP, supported by the information obtained from the RBS spectra in this region. The measurements utilised a proton detector with a solid angle of 30.6 msr and covered with a foil consisting of 5 μm nickel and 12 μm Mylar to stop backscattered ^{3}He ions. The ion incident angle was 0° and the scattering angle 145°. All RBS, PIXE and NRA measurements presented in this work were carried out at the above-mentioned IPP Tandem Laboratory.

Samples H-120 II and IV were subjected to micro-proton-induced X-ray emission (μPIXE) measurements at the Tandem Accelerator Facility of Ruđer Bošković Institute, Zagreb, Croatia [16], to determine the spatial gradients of the net deposition of Pt and W. The samples and the measurement positions are presented in Fig. 8. Positions were chosen based on visible surface modification patterns, together with additional measurement points near the OSP to assess deposition behaviour in this region. At these locations, the superior spatial resolution of μPIXE compared to PIXE enabled a much clearer characterisation of the deposition gradients. The applied proton beam had an energy of 3 MeV and was focused to an 8 × 8 μm^2 spot for each measurement. These individual measurements were combined to construct scan areas of up to approximately 900 × 900 μm^2, with multiple such areas acquired for each sample.

2.3.2. Bulk Mo/W analysis

The FIB cross sections of the W and Mo samples were analysed by SEM (Zeiss Crossbeam 540) to determine their net erosion and deposition. The erosion determination was based on the FIB line-marking technique described in [17]. Additionally, energy-dispersive X-ray spectroscopy (EDX, Oxford Instruments X-Max 80) was performed on the cross section of an L-mode W sample in the vicinity of the strike point to determine the composition of a visually distinct dark surface region after plasma exposure. The EDX measurements were performed at an accelerating voltage of 4 kV and a beam current of 3 nA. All SEM and EDX analyses were performed at Forschungszentrum Jülich GmbH, Jülich, Germany.

3. Analysis of measurement data

3.1. Pt sample analysis - PIXE

Elemental areal densities were derived from the PIXE and μPIXE spectra using the GUPIXWIN software [18]. GUPIXWIN employs a global least-squares fitting procedure that accounts for detector response and peak overlaps. The elements included in the GUPIXWIN analysis for PIXE were Pt, W and Mo, as well as copper (Cu) and zinc (Zn). The detected Pt and Mo originate from the sample materials, while the W is attributed to erosion from surrounding PFCs, potentially including material transported from the main chamber along open field lines to the outer divertor target. The contributions of Cu and Zn are attributed to the accelerator and measurement setup rather than the plasma exposure. Since AUG has operated with a full-W PFC configuration since 2007 [4], Cu is not expected to originate from plasma during the exposure. Instead, Cu most likely originates from the Cu cylinder surrounding the sample in the accelerator analysis chamber [19], which is used to suppress secondary electron contributions to the beam current measurement. Zn, in turn, is observed at the sample edges, where the ion beam may partially intersect the brass (Cu–Zn) sample holder.

The PIXE analysis relies on fitting of selected Siegbahn emission lines in the X-ray spectrum. In this work, the primary choices were Pt L_α (L_3M_4: 9.362 keV, L_3M_5: 9.442 keV) and W L_α (L_3M_4: 8.335 keV, L_3M_5: 8.398 keV) [20], as the L_α lines are the most intense. However, the dominance of Pt on the markers relative to the deposited W complicates the quantification on the marker surfaces. The nearby low-intensity Pt L_ℓ line (L_3M_1: 8.268 keV) partially overlaps with the W L_α lines at the marker positions, contributing to the same energy region. An example spectrum illustrating this behaviour is shown in Fig. 9 from the smaller marker of the H-120 sample II. The figure shows that the Pt L_ℓ line lies close to the peak maximum at ~8.3 keV, whereas the W L_α lines are located on the high-energy slope of the peak. This indicates that the peak is dominated by Pt, while the W contribution is partially masked, which limits the accuracy of the W quantification at the marker positions.

It should be noted that the accuracy of PIXE is limited when quantifying low amounts of deposited material, such as Pt deposited outside the markers and W deposited on the markers, particularly when the material is distributed non-uniformly across the surface. In particular, Pt deposition outside the markers is expected to be more localised in the vicinity of the marker edges rather than uniformly between the markers, which further complicates quantitative analysis when using a relatively large analysis beam area of ~1 × 1 mm^2. Hence, PIXE results for W deposition on the samples and Pt deposition outside the Pt marker regions are not reported in this article. However, the deposition of these elements is examined through the μPIXE results presented in Sections 4.4.1 and 4.4.2. More detailed investigation will be carried out in future work using complementary techniques such as time-of-flight secondary ion mass spectrometry (TOF-SIMS) and SEM. Although the W quantities obtained from the PIXE analysis are not considered sufficiently accurate for quantitative reporting, they can still be used to constrain the W content assumed in the RBS fitting. Where applicable, both the available μPIXE and PIXE results were used for this purpose.

3.2. Pt sample analysis - RBS

The Pt marker thicknesses were obtained by fitting post-exposure RBS spectra using SIMNRA. The simulation parameters were the Ziegler–Biersack electronic stopping model, the Universal nuclear stopping model, asymmetric Gaussian straggling distributions with the Chu-Yang energy-loss straggling model, the Amsel multiple-scattering

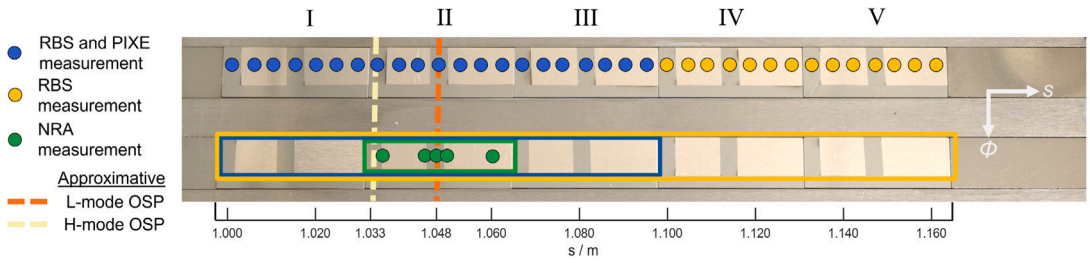

Fig. 7. Photograph of the Pt samples placed on the DIM-II divertor manipulator tile before exposure. The approximate measurement points for PIXE and RBS (blue dots) and for RBS only (yellow dots) are indicated on the upper sample row. On the lower sample row, approximate NRA measurement positions are indicated by green dots. The approximate strike point positions for L-mode (orange dashed line) and H-mode (yellow dashed line) are shown across both sample rows. Rectangles on the lower sample row highlight the sample numbers for which RBS, PIXE, and NRA measurements were performed.

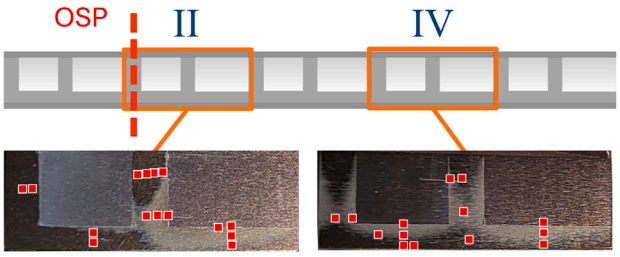

Fig. 8. Samples subjected to μPIXE analysis along with the measurement positions. Positions were chosen qualitatively based on visual inspection as well as knowledge of plasma flows and drifts.

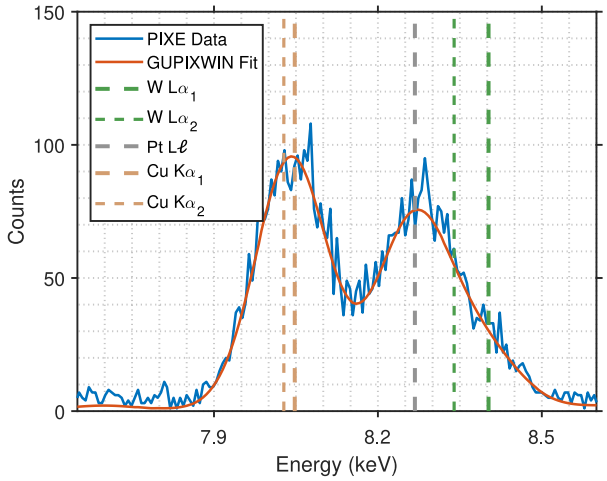

Fig. 9. Example PIXE spectrum from sample II of the H-120 set. The data in the figure is fitted using GUPIXWIN. Dashed lines indicate the Siegbahn lines of interest as well as neighbouring lines that overlap with them.

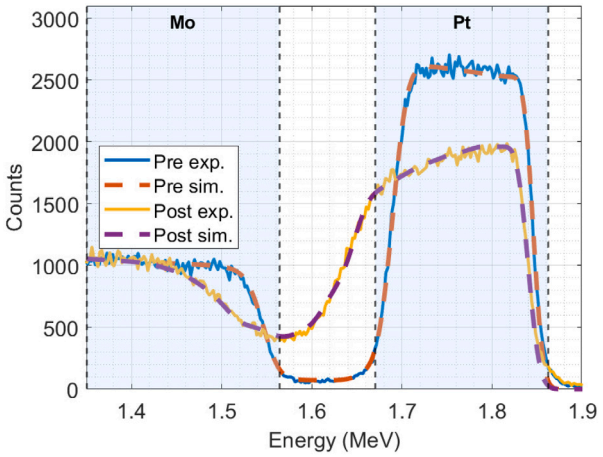

Fig. 10. RBS spectra of the pre- and post-exposure measurements for sample II of the H-120 set, along with the SIMNRA fits of the spectra. The shaded areas labelled "Pt" and "Mo" indicate the pre-exposure areas of Pt and Mo, respectively. After the exposure the Pt peak intensity decreases and becomes broadened. The previously near-zero counts between the Mo high-energy edge and the Pt low-energy edge is filled by a gradually decreasing Mo and increasing Pt contribution, making the separation between the Mo high-energy edge and the Pt low-energy edge less distinct. The Pt high-energy edge is shifted to lower energies and exhibits a less steep increase compared to the pre-exposure case.

model, and screened Rutherford cross-sections using the Andersen screening correction. The accurate straggling option was applied in all simulations. In contrast to the pre-exposure measurements, the spectra include contributions from impurities deposited during the plasma exposure, which shift the Pt signal, while the erosion of Pt reduces the peak width. Additionally, diffusion, material mixing associated with co-deposition and surface roughness may further degrade the initially sharp Pt–Mo interface, leading to broadening of the Pt signal. These effects are observed in Fig. 10, which shows the pre- and post-exposure RBS spectra for the smaller marker on the H-120 sample II, located near the OSP.

In Fig. 10, the thick Pt layer is clearly separated from the Mo substrate in the pre-exposure data with the Mo signal dropping around 1.52 MeV and reaching effectively zero around 1.57 MeV, at energies distinctly below the low-energy edge of Pt at approximately 1.67 MeV. The Pt peak shape is nearly symmetric, indicating little to no mixing between Pt and the underlying Mo. After exposure, the Pt signal shows no clear gap between the Mo edge and the Pt signal low-energy edge. RBS cannot distinguish between the root cause of these spectral features, as both diffusive mixing of materials and surface roughness effects produce similar spectral characteristics [21]. Further analysis using SEM may be required to resolve this ambiguity. Nevertheless, the total amount of Pt can be determined accurately despite this uncertainty [22]. The post-exposure spectra were fitted using a graded multilayer structure, where the Mo concentration increases towards lower energies.

Deposited light elements, e.g., boron (B), carbon (C), D and oxygen (O) on the surface affect the shape of the RBS spectra as the ^{4}He ions lose energy while passing through the impurities on the surface, consequently shifting the Pt peak to lower energies. A small calibration offset was applied when a shift in the spectrum was observed and no NRA measurements were available to quantify deposition of light elements. The exact origin of the energy shift, whether due to surface contamination from light elements or small variations in energy calibration, does not significantly affect the obtained Pt area from the fit. In addition, the detector energy resolution was adjusted during fitting

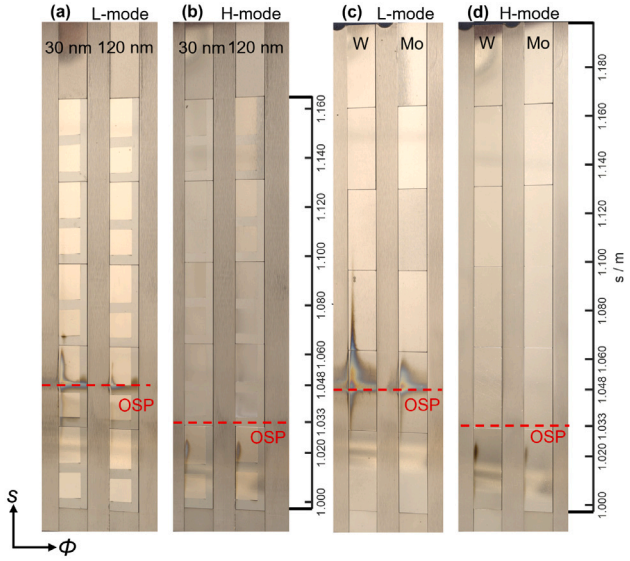

Fig. 11. Photographs of the samples on the divertor tile after exposure, with figures (a) and (b) showing Pt samples subjected to L-mode and H-mode plasmas, respectively, and figures (c) and (d) showing W/Mo samples subjected to L-mode and H-mode plasmas, respectively. A clearly visible dark area appears on the sample II of the L-mode sets in figures (a) and (c). Some of the H-mode markers in (b) are barely visible due to severe erosion during the exposure. Dashed red lines indicate the approximate OSP positions during the exposure.

(typically within 1–3 keV between measurement points, if needed) to match the high-energy Pt edge when contributions from W or light impurities could not explain the observed gradient.

In the obtained RBS spectra, the Pt contribution overlaps with the W signal, which therefore cannot be quantified from the RBS spectra alone. The W content used in the RBS fitting was therefore estimated from PIXE and μPIXE measurements, as described in Section 3.1. Due to the lack of PIXE measurements for samples IV and V, the W contribution for these samples was estimated by extrapolating the W quantities from samples II and III, assuming that W deposition does not vary strongly across the SOL on the spatial scale relevant here. This assumption is supported by μPIXE measurements, which indicate relatively uniform W deposition on sample IV of the H-120 set. The measured W areal densities from the Pt markers were typically of the order of 10^{15} atoms/cm^2 in L-mode and $(10–20) \times 10^{15}$ atoms/cm^2 in H-mode. These corresponded approximately to 1% of the Pt amount for the L-30 samples, below 0.2% for the L-120 samples, 1%–2% for the H-120 samples and approximately 20% for the highly eroded H-30 samples.

3.3. Pt sample analysis - NRA

Due to a measurable shift of the Pt peak to lower energies in the RBS spectra on the markers around the strike point, additional NRA analysis was conducted on samples II in sets L-120 and H-120 to address the potential presence of light elements. The L-mode sample was of particular interest, due to a distinct dark region visible across the samples in the toroidal direction, as shown in Fig. 11(a). In these measurements, a 3 MeV ^{3}He beam was used to detect B, C, D and O via the ^{10}B(^{3}He,p)^{12}C, ^{11}B(^{3}He,p)^{13}C, ^{12}C(^{3}He,p)^{14}N and ^{16}O(^{3}He,p)^{18}F reactions. The corresponding proton peak areas were integrated and converted to elemental areal densities by comparison with calibration measurements from reference samples of known areal density described in [23].

3.4. W and Mo sample analysis - SEM and EDX

After the exposure, the W and Mo samples were analysed using SEM and EDX. Net erosion of the samples was determined by comparing pre- and post-exposure cross section markings using SEM (see Fig. 5). The cross section of the W sample located 17 mm from the edge of sample II in the L-mode sets, around the strike point, was analysed using EDX. Dark regions in the surrounding area, shown in Fig. 11(c), indicate impurity deposition. Similar darkened regions at the same s coordinates in the L-mode samples (Fig. 11(a) and (c)) and the H-mode samples (Fig. 11(b) and (d)) may indicate a common origin.

4. Experimental erosion and deposition results

4.1. Net erosion of Pt markers

The net erosion rate profiles of the Pt markers obtained using RBS and PIXE show good quantitative agreement, as shown in Fig. 12. The consistency between these two independent ion beam analysis techniques increases confidence in the observed erosion profiles and suggests that the results are not strongly affected by technique-specific systematic uncertainties. The erosion rates in the L-mode experiments are low with total erosion of the order of a few nanometers over the five L-mode discharges of the experiment.

Fig. 12(a) shows that the net erosion increases around the OSP towards the near SOL region (approximately 0–20 mm from the OSP in the positive s direction), followed by an approximately 20 mm wide plateau. Beyond approximately 40 mm from the OSP, the erosion increases again towards the far SOL. This plateau likely corresponds to re-deposition of eroded material from the SOL region that is transported towards the OSP prior to re-deposition. Due to the vertical target geometry of AUG, the surface normal of the outer target points towards the separatrix in the SOL, such that, on average, the eroded neutrals launched from the target are ionised on an inner flux surface and return to the target with the plasma flow closer to the strike point with respect to their original erosion site. A further contribution to the transport of ionised eroded particles towards the strike point arises from the radial $\vec{E}_\theta \times \vec{B}$ drift. Conversely, some deposited material could be transported from the strike point towards the SOL due to changes in the local electric field, which can reverse the direction of the $\vec{E}_\theta \times \vec{B}$ drift [24]. The erosion and re-deposition cycle may occur multiple times for individual particles, leading to a progressive displacement of material along the surface (also referred to as “walking”) [25].

Net erosion data for the L-120 samples shown in Fig. 12(b) is presented by averaging the measurements from the smaller markers to approximate the value at the central position corresponding to the pre-exposure measurement point, while for the larger marker only the central measurement point was retained to allow direct comparison between pre- and post measurements. This approach was adopted to remove the oscillatory features observed in the original RBS and PIXE results, shown in grey in Fig. 12(b), which are believed to arise from pre-exposure thickness variations of the thicker Pt marker layers, originating from the manufacturing of the samples. This interpretation is supported by the pre-exposure measurements shown in Fig. 6, which indicate a systematic increase in the thickness of the 120 nm markers on a single sample. The same trend is reflected in the untreated net erosion data, where both the smaller and larger markers exhibit reduced apparent net erosion towards the SOL. The influence of such thickness variations is expected to be most pronounced for the L-120 marker set due to the comparatively low net erosion during the L-mode exposure, whereas in H-120 the substantially higher and more pronounced erosion largely mask the effect. However, as the pre-exposure measurements were performed at only a single position per marker, this interpretation remains speculative. With this treatment, a more consistent erosion profile is obtained, which is in better agreement with the trends observed for the L-30 marker set.

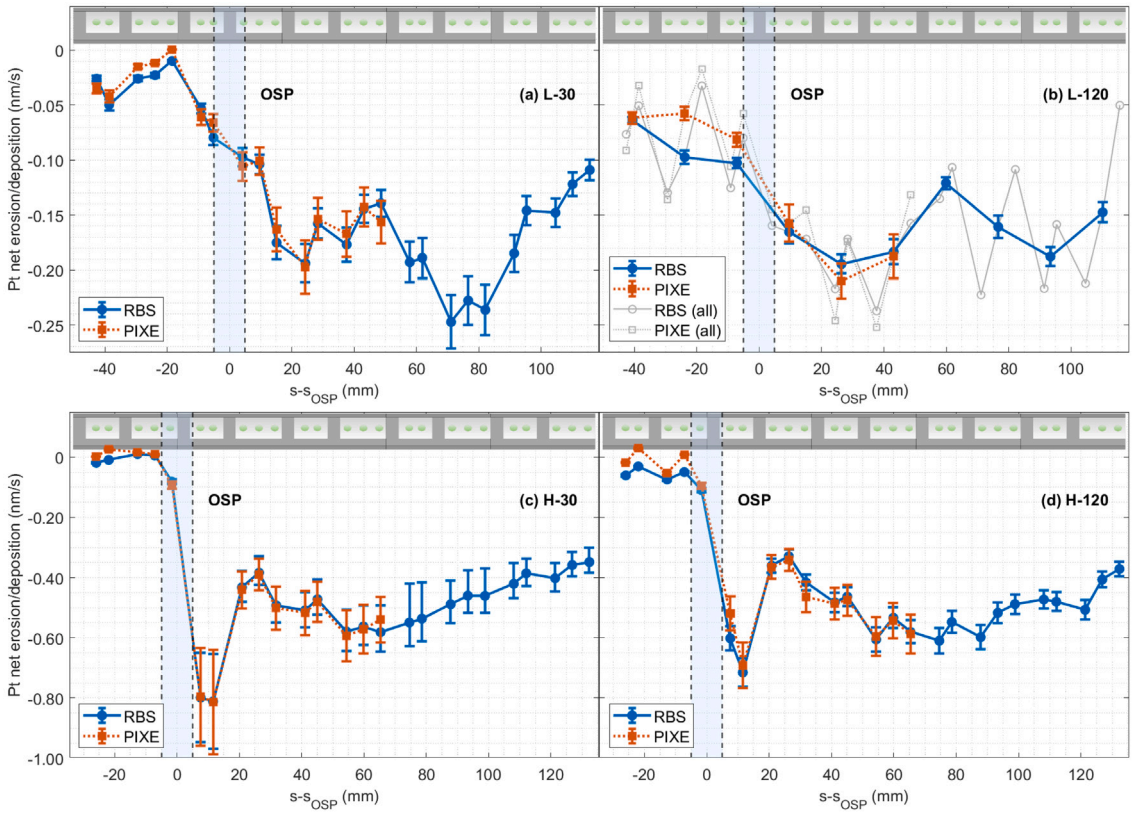

Fig. 12. Net erosion/deposition rate profiles obtained with RBS (blue) and PIXE (orange) for (a) L-mode 30 nm, (b) L-mode 120 nm, (c) H-mode 30 nm and (d) H-mode 120 nm Pt markers exposed to plasma. Negative values indicate net erosion and positive values net deposition. In (b), for the smaller markers, the results are averaged over two measurement points to approximate the centre position of the marker. For the larger Pt markers, only the central measurement point is included, as it corresponds to the available pre-exposure measurement position. The original unaveraged L-120 datasets are shown in grey on the background. The shaded region labelled "OSP" indicates the approximate OSP position during the discharges. Green points overlaid on the Pt sample row illustration indicate the measurement positions.

In H-mode, Fig. 12(c) and (d) show 2–6 times higher net erosion rates than in L-mode. The erosion is pronounced near the OSP, with a likely deposition peak appearing in the near SOL and causing a local decrease of the net erosion rate at a distance of 20–40 mm from the strike point. This behaviour can be attributed to the same transport and re-deposition mechanisms discussed for L-mode. In H-mode, however, the higher plasma density and temperature lead to shorter ionisation mean free paths, resulting in enhanced prompt re-deposition of particles eroded near the OSP. The higher plasma density and steeper temperature gradients in the divertor volume in H-mode may also lead to stronger local electric fields and thus increased radial $\vec{E}_\theta \times \vec{B}$ drift velocities, enhancing cross-field transport along the surface. The net erosion rate in this high-deposition region 20–40 mm from the strike point is, however, still ~3 times higher compared to the same region in L-mode.

4.2. Error estimation

The uncertainty estimation procedure for the post-exposure RBS measurements follows that described in Section 2.2. with an additional contribution arising from the estimation of the W content used in the RBS fitting. As described in Section 3.1, the W contribution used in the RBS fits was estimated primarily from the available μPIXE measurements on neighbouring Mo surface regions, where the W signal is not affected by overlap with Pt. Preliminary SDTrimSP [26] calculations did not indicate significant differences in the reflection coefficients of W on Pt and Mo surfaces, supporting the use of neighbouring Mo measurements to estimate the W content on the Pt markers, although local spatial variations in W deposition cannot be excluded. To account for the possibility that the actual W content on the Pt markers differs from this estimate, the RBS fits were repeated using alternative W amounts obtained from the corresponding PIXE measurements on the Pt marker surfaces. The resulting variation in the fitted Pt amount was incorporated into the uncertainty analysis.

The effect of the assumed W content on the RBS fits was most pronounced for the H-30 samples due to the comparatively high W-to-Pt ratio, whereas for the H-120 samples the corresponding contribution was substantially smaller because of the larger Pt inventory relative to the deposited W. In the L-mode samples, the deposited W amounts were sufficiently low that this contribution was considered negligible. The uncertainty associated with the assumed W content was evaluated separately for each measurement point and incorporated into the corresponding RBS uncertainty estimate.

For PIXE, where the detector is calibrated using RBS reference measurements, the overall accuracy has been reported to be in the range of 5%–10% [19]. In this work, a representative value of $u = 10\%$ was used for PIXE. The total relative uncertainty was then calculated according to Eq. (1).

4.3. Deposition of impurities observed using NRA

Fig. 13(a) and (b) present the amounts of light elements measured with NRA on the surfaces of samples II of L-120 and H-120, with the approximate measurement positions indicated in the top-right inset in (a). The position between the markers in the vicinity of the strike point in Fig. 13(a) and its neighbouring locations correspond to the darkened region around the strike point in Fig. 11(a). Between the markers, the deposition of all four observed elements appears to be

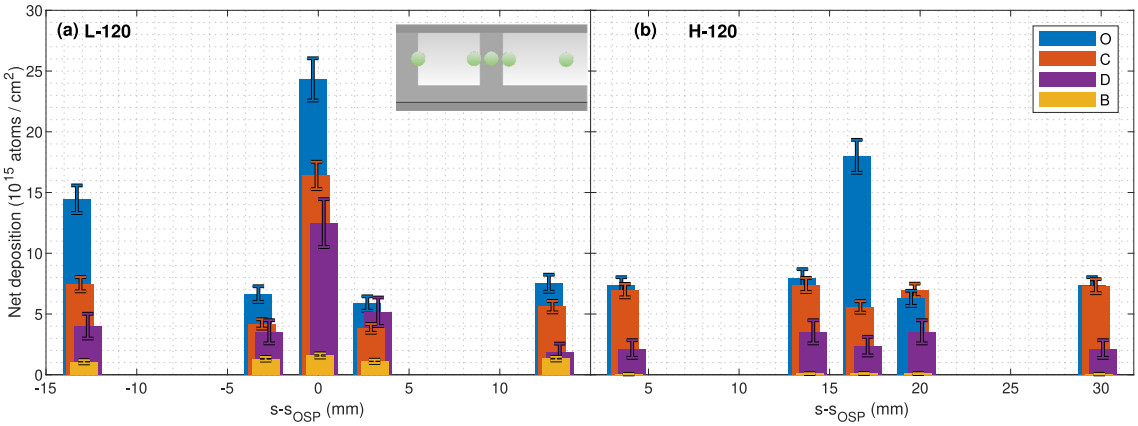

Fig. 13. Net deposition rates of light impurities (O, C, B) and D on the (a) L-120 and (b) H-120 sample II, obtained using NRA. The bar diagrams are grouped along the *s*-axis according to their spatial measurement positions relative to the approximate OSP location. The measurement positions on sample II are indicated as green dots in the inset in figure (a). The cluster of three measurement points near the sample centre is included to provide a more detailed view of the light impurities in the darker region around the OSP, visible in Fig. 11(a). In figure (b), the measurement positions are identical to those of the L-mode sample shown in (a). The deposition of D is close to zero at all measurement positions in (b) and is therefore not visible in the diagrams.

highest. This location lies in the immediate vicinity of the OSP, where the particle flux is typically highest. The D content is relatively uniform across the sample in L-mode, whereas it remains very low in the H-mode sample and is comparable to the measurement uncertainty. This behaviour is consistent with reduced D retention at elevated surface temperatures, as retention has been reported to increase at lower irradiation temperatures due to enhanced trapping in defects [27].

The O levels appear to be highest on the Mo surfaces, which may reflect the lower oxidation resistance of Mo compared to Pt. However, exposure of the samples to ambient air before and after the plasma exposures may also contribute to the observed O content. Therefore, the measured O content cannot be assumed to originate solely from deposition during the experiment. Similarly, the measured C inventory should be interpreted with caution, since the carbon content of the samples prior to plasma exposure was not determined and the observed C cannot therefore be unambiguously attributed to deposition occurring during the experiment.

The high deposition rate observed in the PFR in Fig. 13(a) may also be associated with the dark surface region visible in Fig. 11(a). The error bars shown in the figure were obtained by propagating uncertainties associated with the calibration procedure, beam charge normalisation, and counting statistics of both the calibration and sample spectra according to Eq. (1). The resulting relative uncertainties range from approximately 7% for the strongest signals up to about 50% for measurements with low counting statistics, such as the deuterium concentrations measured on the H-120 samples.

4.4. Deposition of Pt and W on Mo - μPIXE

4.4.1. Deposition of Pt

Fig. 14(a) and (b) present Pt deposition patterns measured with μPIXE on the Mo surfaces surrounding the Pt markers on the H-120 samples II and IV, respectively. As observed in Fig. 14(a), elevated Pt deposition is found for a group of measurement points located downstream of the larger Pt marker, at toroidal positions of ~0–3 mm and a distance of ~26 mm from the OSP, where the deposition decreases with increasing distance from the marker. A second region of enhanced deposition is observed for measurement points located at toroidal positions of ~4 mm and distances of ~16–19 mm from OSP, suggesting a combination of transport mechanisms driving the migration of the eroded particles, including entrainment with the parallel plasma flow and the radial migration mechanisms discussed in Section 4.1. Measurements taken along the toroidal mid-point between the markers (toroidal positions of ~9–10 mm at distances of ~15–19 mm) from the OSP show

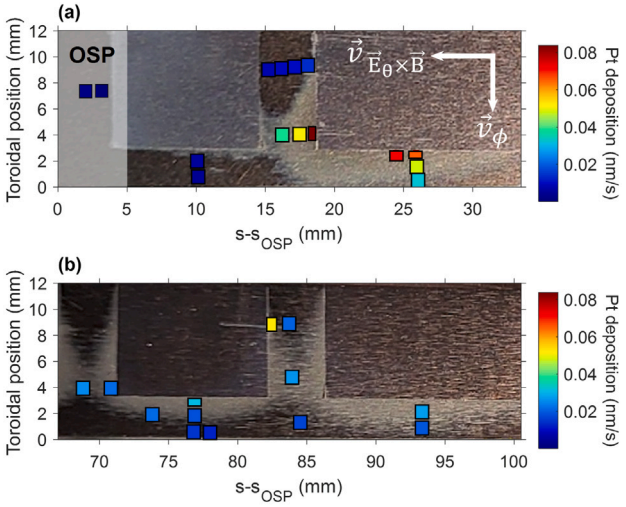

Fig. 14. Heatmap of Pt deposition rate on the Mo surfaces of the H-120 (a) sample II and (b) sample IV based on μPIXE measurements. In (a) the shaded white region represents the approximate OSP position. The sizes of the measurement regions are not uniform, as areas overlapping the Pt markers were excluded from the analysis, resulting in smaller effective scan areas at some locations.

only a fraction of the deposited Pt, approximately a factor of 4–6 lower than in the downstream region, supporting the postulated strong role of the parallel plasma flow in migration of the eroded Pt.

Downstream from the smaller Pt marker in Fig. 14(a), at measurement points approximately at toroidal positions of ~1–2 mm and a distance of ~10 mm from the OSP, the deposition remains low. This is somewhat unexpected, as high net erosion is measured at this marker, and some deposition outside the marker might therefore be anticipated. One possible explanation is a high prompt re-deposition rate of eroded particles back onto the marker surface before significant toroidal transport occurs. In such a case, only a limited fraction of the eroded Pt would reach the neighbouring Mo surfaces, resulting in low Pt deposition outside the marker despite the substantial erosion measured at the marker itself. In this case, modifications of the marker surface itself, such as a decrease in net erosion in the downstream direction, could occur. However, this cannot be directly assessed with the available experimental data, as no pre-exposure toroidal thickness

profile is available, and will be addressed in future modelling efforts. In addition, Pt deposited on the surrounding Mo surface may be more readily re-eroded in the vicinity of the OSP due to the higher particle fluxes and temperatures in this region, thereby reducing the net deposition outside the marker.

In addition, the two measurement points located in the OSP region (toroidal distance ~7 mm and ~3–4 mm from the OSP) show no statistically significant Pt deposition. Similarly to the cases downstream of the smaller marker, a high rate of prompt re-deposition may cause sputtered atoms to return to the marker surface before notable radial migration onto the Mo surface. Part of this behaviour may also be associated with local variations in the electric field, which could alter the direction of the radial $\vec{E}_\theta \times \vec{B}$ drift and drive eroded particles back towards the SOL.

Fig. 14(b) also shows a decrease in the deposition rate as a function of distance from the Pt markers at measurement point groups located at distances of ~77 mm and ~93 mm from the OSP. In this sample, the Pt deposition is more uniform, with values ranging between 0.01–0.03 nm/s, except for the measurement at the approximate toroidal mid-point between markers (toroidal position of ~9 mm at a distance of ~83 mm from the OSP). The more uniform deposition may be a consequence of longer ionisation mean free paths at larger distances from the OSP, where lower particle fluxes and temperatures may allow eroded Pt particles to travel further before ionisation. This could result in a broader deposition profile and reduced localisation of deposited material near the markers.

4.4.2. Deposition of W

Fig. 15 visualises the W deposition rates for the H-120 samples II and IV, obtained from the same μPIXE measurement positions as those used for the Pt deposition analysis shown in Fig. 14. In Fig. 15(a), the W deposition, expectedly, does not exhibit a similar gradient as a function of distance from the Pt markers. However, unexpected similarities to the spatial distribution of Pt deposition are observed, e.g., at the toroidal mid-point between the markers (toroidal position ~9 mm and a distance of ~15–19 mm from the OSP) where the W deposition is approximately a factor of two lower than in the corresponding downstream region (toroidal position ~4 mm and a distance of ~16–19 mm from the OSP). This observation deviates from the anticipated behaviour, as the majority of the tungsten is expected to originate from its content in the divertor plasma and, on a local scale, the neighbouring W surfaces from which it is transported on to the samples along the parallel plasma flow. Based on this, the W deposition would be expected to be toroidally more uniform and higher closer to the upstream edge of the samples than in the downstream region. This discrepancy may be related to differences in surface morphology. The lighter colouring of the Mo surfaces around the markers in Figs. 14 and 15 may indicate increased surface roughness, which has been shown to affect sputtering and re-deposition processes, leading to reduced effective sputtering within surface features [28,29]. Such an effect would also play an enhancing role, along with the parallel plasma flow, in the toroidal distribution of the Pt deposition in the same region, discussed in Section 4.4.1. This highlights the need for further investigation of the surface morphology using SEM or similar methods.

The low W deposition downstream of the smaller marker in Fig. 15(a), at a toroidal position of ~1–2 mm and a distance of ~10 mm from the OSP, may be associated with differences in surface morphology and the lower net deposition expected closer to the OSP. Little to no visible surface modification is observed in this area, suggesting a smoother surface from which deposited material may be more readily re-eroded compared to regions exhibiting pronounced surface features discussed above. Furthermore, the higher particle fluxes and temperatures in the vicinity of the OSP may enhance re-erosion, thereby reducing the net accumulation of deposited W.

On sample IV in Fig. 15(b), the W deposition rate is relatively uniform with most values in the range of ~0.03–0.04 nm/s. This indicates

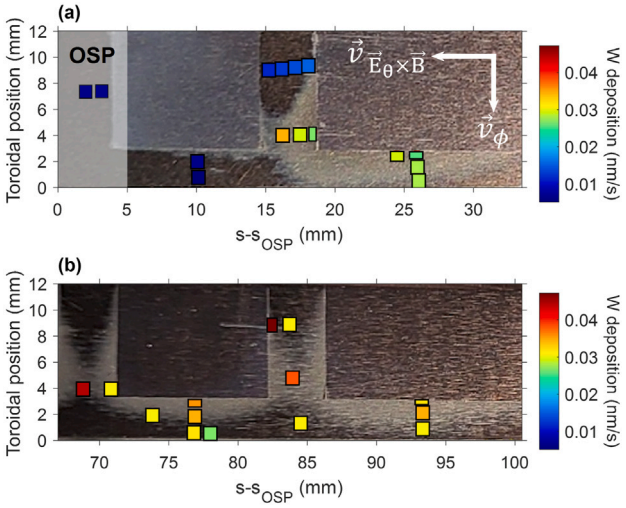

Fig. 15. Heatmap of the W deposition rate on the Mo surfaces of the H-120 (a) sample II and (b) sample IV based on μPIXE measurements. In (a) the shaded white region represents the approximate OSP position. The sizes of the measurement points are not to scale.

that W deposition may not be dominated solely by local sources, i.e., by the divertor tile in which the samples are mounted, but instead reflects transport along the SOL field lines from spatially distributed erosion sites elsewhere in the machine. In addition, the contribution from local W sources is expected to be lower at the location of sample IV than at sample II, as the distance from the OSP is larger and the local plasma conditions are cooler, resulting in reduced W erosion. However, surface modifications may promote increased local re-deposition within surface features and lead to non-uniform deposition along the toroidal direction.

Lower deposition of W is observed downstream of the smaller marker (toroidal position of ~1 mm at a distance of ~78 mm from the OSP), corresponding to the visibly darker surface region. The highest deposition rate is observed at the toroidal mid-point between the markers, i.e., at the same measurement position that also exhibits the highest Pt deposition on this sample, where a scratch-like feature is observed on the Pt marker and may be associated with reduced effective sputtering and enhanced local re-deposition, as discussed above. Its origin cannot be determined from the present data, but it may be related to localised surface modification processes, such as arcing or other non-sputtering mechanisms. Further investigation, for example by SEM, would be required to identify its origin.

4.5. Erosion and deposition analysis on Mo and W samples - SEM and EDX

Due to the relatively low net erosion observed on the W and Mo samples, which remained well below the ~1 μm spacing of the FIB line markings, estimated erosion depths could only be determined for the H-mode Mo samples II and III from the cross sections located 17 mm from the sample edge at the centre of the sample, as shown in Fig. 4. Ne injection was intended to enhance erosion on the samples during the exposure, but its effect was negligible due to the technical difficulties discussed in Section 2. The cross section of sample II is located approximately at the strike point, while the cross section of sample III is in the near SOL, approximately 33.5 mm from the OSP. The estimated erosion depths are of the order of 80 nm on sample II and 50 nm on sample III, corresponding to erosion rates of approximately 2.5 nm/s and 1.6 nm/s, respectively.

Elemental depth profiles measured by EDX from the cross section at the centre of the L-mode W sample II are presented in Fig. 16. The Ga

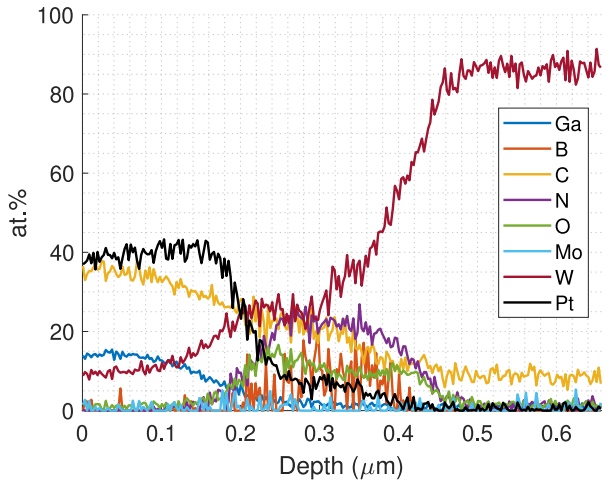

Fig. 16. EDX depth profiles of selected impurities on the W sample II exposed to L-mode plasma. The Ga concentration originates from Ga ion implantation during FIB preparation, while the Pt concentration arises from the protective/conducting Pt+C layer deposited after the exposure.

concentration originates from Ga ion implantation during FIB preparation, while the Pt concentration arises from the protective/conducting Pt+C layer deposited during sample preparation after the plasma exposure and not from eroded Pt from the Pt markers. W is the bulk material of the sample, and its concentration approaches 100% with increasing depth.

Similar impurities to those observed on the Pt samples are found, including B, C, and O. The O concentration appears to exceed that of B over much of the analysed depth range, agreeing with the NRA measurements of the total O and B contents on the Pt samples presented in Fig. 13, although the interpretation is complicated by the relatively noisy B profile. A high concentration of nitrogen (N) is also observed beneath the Pt layer. Since nitrogen seeding is routinely applied in AUG for divertor power load control via radiative cooling, its presence in the post-exposure analysis is not unexpected.

5. Discussion and conclusions

In this paper, material erosion and migration at the outer divertor target of AUG were investigated. Identical sets of Pt samples, used as a proxy for W, together with bulk W and Mo samples, were exposed to L- and H-mode D plasmas with minor Ne seeding in the OSP region. The exposures were carried out using the DIM-II divertor manipulator and were performed on consecutive experimental days under a similar magnetic configuration, providing a controlled environment for erosion studies in a tokamak. Afterwards, the Pt samples were subjected to extensive ion beam analysis and the bulk W and Mo samples to SEM and EDX analysis. The study provided data on the net erosion of the samples together with migration and deposition of the eroded material, as well as accumulation of light impurities on surfaces near the OSP in AUG.

For the Pt markers, well-defined net erosion profiles were obtained around the OSP with RBS measurements, the validity of which was supported by complementary PIXE analysis. The net erosion rates in H-mode were approximately a factor of 2–6 higher than in L-mode. In H-mode, a distinct erosion peak was observed in the vicinity of the strike point, followed by a deposition region in the near SOL at distances of approximately 20–40 mm from the OSP, and increased net erosion further into the SOL. In contrast, in L-mode, net erosion near the strike point was less distinct, while the main erosion peaks were shifted further into the SOL at distances of approximately 30 mm and 80 mm from the strike point. These qualitative differences may suggest differences in the significance of prompt re-deposition and re-erosion of deposited Pt on the marker surfaces near the strike point. Analysis of the RBS spectra also indicated less distinct interfaces between the Pt markers and the Mo substrate following the plasma exposure, especially on the H-120 set samples II and III, potentially due to diffusion, mixing of materials or increased surface roughness.

The μPIXE analysis, which was specifically targeted at visually observable surface modifications on the Pt samples exposed to H-mode plasmas, provided spatial information on migration and deposition of high-Z elements outside the source regions near the OSP. In particular, the observed deposition pattern of Pt downstream of the marker regions suggests migration consistent with the parallel plasma flow with a radial shift towards the OSP due to the ionisation distribution of the eroded neutrals and the $\vec{E}_\theta \times \vec{B}$ drift. Around the marker closest to the strike point, deposition was not observed, which may indicate a strong role of prompt re-deposition of Pt back onto the marker surface and/or efficient re-erosion of Pt deposited on the surrounding Mo surface in the region of the highest plasma temperature and ion flux, as well as potential changes in the radial drift mechanisms due to local variations in the electric field. In addition, the μPIXE measurements showed a non-uniform W surface distribution, with enhanced accumulation of deposited material observed in regions exhibiting visible surface modifications, which may be related to reduced effective sputtering and enhanced local re-deposition within surface features.

Compared to the earlier Au-marker studies [11,12], the larger total marker area together with the denser spatial coverage of the measurements enabled a more detailed characterisation of the net erosion profiles around the OSP and provided more detailed information on material migration and deposition outside the marker regions.

Overall, the results indicate that both prompt re-deposition and SOL transport, together with surface modifications, play a key role in shaping impurity deposition patterns at the outer target, and provide experimentally derived reference data for further studies of erosion and migration phenomena using numerical simulations. Further experimental investigations are still required to resolve the role of surface modifications in the formation of the observed high-deposition regions of Pt and W using SEM. In addition, more detailed characterisation of deposition will be pursued with extensive TOF-SIMS measurements on a broader set of samples. Dedicated modelling studies of the experiment will also be conducted using ERO2.0 and SDTrimSP to assess the significance of the different postulated physical phenomena for the observed net erosion and material migration, as well as the validity of extrapolating observations made with the Pt markers to W PFCs.

CRediT authorship contribution statement

S. Saari: Writing – original draft, Visualization, Investigation, Formal analysis, Conceptualization. **A. Hakola:** Writing – review & editing, Supervision, Investigation, Funding acquisition, Conceptualization. **J. Karhunen:** Writing – review & editing, Supervision, Investigation, Conceptualization. **K. Krieger:** Writing – review & editing, Supervision, Resources, Project administration, Investigation, Data curation, Conceptualization. **M. Rasinski:** Investigation, Formal analysis, Conceptualization. **M. Balden:** Writing – review & editing, Investigation. **C. Baumann:** Writing – review & editing, Investigation, Formal analysis, Conceptualization. **I. Bogdanović Radović:** Writing – review & editing, Investigation, Formal analysis. **S. Gouasmia:** Investigation, Formal analysis. **M. Mayer:** Writing – review & editing, Resources, Investigation, Formal analysis. **G. Provatas:** Investigation, Formal analysis. **J. Romazanov:** Conceptualization.

Declaration of competing interest

The authors declare that they have no known competing financial interests or personal relationships that could have appeared to influence the work reported in this paper.

Acknowledgements

This work has been carried out within the framework of the EUROfusion Consortium, funded by the European Union via the Euratom Research and Training Programme (Grant Agreement No 101052200 — EUROfusion). Views and opinions expressed are however those of the author(s) only and do not necessarily reflect those of the European Union or the European Commission. Neither the European Union nor the European Commission can be held responsible for them.

Data availability

Data will be made available on request.

References

[1] V. Philipps, J. Nucl. Mater. 415 (2011) S2–S9.
[2] D. Naujoks, et al., Nucl. Fusion 33 (1993) 581.
[3] A. Hakola, et al., Nucl. Fusion 61 (2021) 116006.
[4] R. Neu, et al., Nucl. Mater. Energy 438 (2013) S34–S41.
[5] H. Zohm, et al., Nucl. Fusion 64 (2024) 112001.
[6] A. Herrmann, et al., Fusion Eng. Des. 98–99 (2015) 1496.
[7] S. Kashiwaya, et al., 2D Mater. 12 (2025) 033001.
[8] A.I.G. McLaughlin, et al., Br. J. Ind. Med. 3 (1946) 183–186.
[9] A. Büttner, et al., Thin Solid Films 662 (2018) 41–46.
[10] J. Romazanov, et al., Phys. Scr. T170 (2017) 014018.
[11] A. Hakola, et al., Nucl. Mater. Energy 25 (2020) 100863.
[12] S. Saari, et al., Nucl. Mater. Energy 45 (2025) 102032.
[13] M. Mayer, et al., Nucl. Fusion 60 (2020) 025001.
[14] M. Mayer, SIMNRA User's Guide, Max-Planck-Institut für Plasmaphysik, 2014, Version 7.03.
[15] Joint Committee for Guides in Metrology (JCGM), Evaluation of Measurement Data — Guide to the Expression of Uncertainty in Measurement (GUM 1995 with Minor Corrections), JCGM 100:2008, BIPM, IEC, IFCC, ILAC, ISO, IUPAC, IUPAP, OIML, 2008.
[16] M. Jakšić, et al., Nucl. Instr. Methods B 539 (2023) 120–126.
[17] M. Rasiński, et al., Nucl. Mater. Energy 37 (2023) 101539.
[18] J.L. Campbell, et al., The GUPIX Manual and User-Guide, Version 3.0.3, University of Guelph, 2021.
[19] S. Werner, Kalibration eines Röntgendetektors für PIXE und erste Messungen an plasmaexponierten Proben, TU München, 2021.
[20] X-Ray Transition Energies Database, 2026, https://www.nist.gov/pml/x-ray-transition-energies-database, Last updated September 2005, (Accessed May 2026).
[21] A. Crespo-Sosa, et al., Phys. Rev. B 53 (1996) 14795.
[22] M. Mayer, et al., Nucl. Instrum. Methods B 385 (2016) 65–73.
[23] K. Krieger, et al., Nucl. Mater. Energy 46 (2026) 102070.
[24] H.Q. Wang, et al., Phys. Rev. Lett. 124 (2020) 195002.
[25] T. Abrams, et al., Mater. Res. Express 10 (2023) 126503.
[26] A. Mutzke, et al., SDTrimSP Version 6.00, IPP Report, 2019.
[27] L. He, et al., Nucl. Fusion 65 (2025) 016056.
[28] A. Eksaeva, et al., Nucl. Mater. Energy 19 (2019) 13–18.
[29] A. Kreter, et al., Plasma Phys. Control. Fusion 50 (2008) 095008.